Physica Medica 65 (2019) 157–166

Contents lists available at ScienceDirect

Physica Medica

journal homepage: www.elsevier.com/locate/ejmp

Original paper

A model-based algorithm to correct for the loss of backscatter in superficial X-ray radiation therapy

Jeffrey R. Harwood*, Flavio E. Nelli

Andrew Love Cancer Centre, University Hospital Geelong, 70 Swanston St, Geelong, Vic 3220, Australia

ARTICLE INFO

Keywords:
Backscatter
Superficial X-ray therapy
Gafchromic film
Monte Carlo

ABSTRACT

Dosimetry protocols for superficial X-rays prescribe the determination of kerma on the surface of a phantom through the use of a backscatter factor (B_w) that accounts for the effect of phantom scatter. B_w values corresponding to full-scatter phantoms are provided by these protocols. In practice, clinical situations arise wherein there is insufficient scattering material downstream, resulting in published B_w values that overestimate the amount of occurring scatter.

To provide an accurate dose calculation the backscatter values need to be corrected for any reduction in scattered radiation. Estimating the change of B_w in situations with incomplete backscatter has previously been achieved by direct measurements or Monte Carlo modelling. For increasing the accuracy of clinical dosimetries, we developed a physical model to deduce an algorithm for calculating backscatter factors in situations with reduced downstream scattering medium. The predictions of the model were validated by comparison with published data, Monte Carlo simulations and film-based measurements for beams with a half-value layer of 0.8, 2 and 4 mm Al.

Our algorithm accurately predicts the effect of partial scatter conditions with suitable precision. Its reliability, combined with the simplicity of calculation, makes this methodology suitable to be incorporated into routine clinical dosimetry. The algorithm's underlying physical model provides an intuitive understanding of the effects of field size and beam energy on backscatter reduction, permitting a rational management of this effect.

1. Introduction

Superficial X-ray radiation therapy (SXRT) utilises low-energy X-rays. The low-penetrating nature of superficial X-rays means most of the dose is delivered near the surface of the treated region, making them suitable for treating a variety of malignant or benign skin conditions.

Dosimetry protocols for superficial X-rays, such as those provided by the Institution of Physics and Engineering in Medicine and Biology (IPEMB) and the American Association of Physicists in Medicine Radiation Therapy Committee Task Group 61 (TG-61), state that reference dosimetry for determining dose to water on a phantom surface is performed free-in-air for low energy X-rays with tube potentials less than or equal to 100 kV [1–3]. The same methodology can be used for tube potentials up to 300 kV [1–3].

The ionization chambers used for SXRT reference dosimetry are calibrated in terms of air kerma free-in-air. Air kerma free-in-air is converted to water kerma free-in-air through multiplication by the ratio for water-to-air of the mean mass energy-absorption coefficients averaged over the incident photon spectrum, $(\bar{\mu}_{en}/\rho)^{w}_{air}$ (values of $(\bar{\mu}_{en}/\rho)^{w}_{air}$ are supplied by dosimetry protocols such as TG-61). Water kerma on the surface of a phantom is determined by the application of a backscatter factor, B_w, which accounts for the effect of phantom scatter. Absorbed dose to water is equivalent to water kerma provided that charged particle equilibrium is preserved. Backscatter values corresponding to fully developed backscatter conditions are available from major clinical dosimetry protocols [1–3]. Published values are generally utilised in favour of direct measurement as direct measurements of backscatter values are challenging in the clinical environment [4,5].

Machine outputs are typically calibrated in terms of water kerma in-air, calling for the use of the methodology described above for clinical dosimetries. Clinical situations arise wherein there is insufficient downstream scattering material, resulting in the published backscatter values overestimating the amount of occurring scatter. Commonly encountered situations of this nature include those where shielding is used to protect underlying tissue, such as treatments to the ear, nose and lip, treatments to sites with insufficient underlying tissue, such as the hand, and treatments to sites with shallow underlying bone (due to the differential X-ray absorption in bone resulting in reduced backscatter),

* Corresponding author.
E-mail address: jeffharwoodromp@gmail.com (J.R. Harwood).

https://doi.org/10.1016/j.ejmp.2019.08.018
Received 28 January 2019; Received in revised form 29 May 2019; Accepted 23 August 2019
Available online 05 September 2019

such as the scalp [5,6]. To provide an accurate dose calculation, the published backscatter values need to be corrected for the loss of scattering material.

The need to correct for the loss of backscatter is highlighted in the recent ACPSEM position paper, however, no methodology for this correction is provided [5]. Estimations of the change of B_w in situations with incomplete backscatter have been achieved by direct measurements or by Monte Carlo (MC) modelling, however, these methods lack the simplicity and versatility required for usage in the everyday clinical environment [6–11]. Calculation methodologies based on fitting complex exponential functions to empirical data have been published [11]; this approach lacks an underlying physical model supporting its mathematical form and the dependences of its functional parameter on experimental variables as field size, HVL, etc. The absence of an underlying physical model prevents the extension of the algorithm to different situations as multiple layers, extension suited for modelling underlying bones.

Additionally, there are an increasing number of superficial machines in dermatologic clinics and these units often have no direct physics support [12–15] appealing for simple, yet precise, dosimetric calculation algorithms.

For these reasons, a calculation algorithm to correct for the loss of backscatter in superficial X-ray radiation therapy was developed.

The algorithm introduced in this work is based on a simple semi-empirical model of the transport of photon radiation. The predictions of the model were tested through comparison with findings from MC modelling, film measurements and previous published data. The model-based algorithm is being used in clinical dosimetry calculations at Andrew Love Cancer Centre, University Hospital Geelong.

In this paper we will outline the physical principles used to deduce the calculation algorithm for assessing the effect of incomplete scatter and present two methods for validating the accuracy of the calculation algorithm.

2. Materials and methods

2.1. Calculation algorithm

2.1.1. Homogenous phantoms

We developed a physical model to deduce an algorithm for calculating the backscatter factor in situations with reduced scattering medium. This model is graphically depicted in Fig. 1. A full deduction is presented in this section, to enable the reader to adopt the model for use in their clinics.

In a water phantom under full backscatter conditions (Fig. 1(ii)), the dose to point **a** is the water kerma free-in-air at **a**, $K_{\mathbf{a}}$, multiplied by the water backscatter factor, B_w:

$$D_{\mathbf{a}} = K_{\boldsymbol{a}} \cdot B_w \tag{1}$$

The scatter contribution to dose at point **a**, S_a, is given by:

$$S_{\mathbf{a}} = K_{\boldsymbol{a}} (B_w - 1) \tag{2}$$

For X-rays generated using between 60 kV and 300 kV, the dominant interaction in water is the Compton effect. Below 60 kV the photoelectric effect becomes the dominant interaction. The maximum range of the electrons produced by these beams, in water, is less than 0.8 mm and the characteristic photoelectric emissions in water are of very low energy, negligibly contributing to dose at distance [16]. The Compton effect is the dominant source of photons that build up the backscattered radiation. It is therefore sound to treat the scattered radiation as if it were made up of single-scattered photons carrying essentially the same energy as the impinging radiation, as the mean energy loss of Compton-backscattered photons is insignificant at superficial X-ray beam energies (see Appendix 1).

In situations where there is an incomplete scatter region we need to account for the missing scatter. This situation is shown in Fig. 1(i), where we need to account for the missing scatter, $S_{\mathbf{a}}^{\beta}$, resulting from the missing material of region $\boldsymbol{\beta}$ (Fig. 1(ii)) in order to determine the scatter from region $\boldsymbol{\alpha}$ alone.

We define the scatter contribution to point **a** from regions $\boldsymbol{\alpha}$ and $\boldsymbol{\beta}$ as $S_{\mathbf{a}}^{\alpha}$ and $S_{\mathbf{a}}^{\beta}$. Assuming the backscattered radiation is made up of single-scattered photons, the sum of the scatter from these two regions equals the full-scatter contribution, so:

$$S_{\mathbf{a}} = S_{\mathbf{a}}^{\alpha} + S_{\mathbf{a}}^{\beta} \tag{3}$$

We estimate $S_{\mathbf{a}}^{\beta}$ as the scattered dose at point **b** occurring from region $\boldsymbol{\beta}$, $S_{\mathbf{b}}$, transported upstream through region $\boldsymbol{\alpha}$ to reach point **a** (Fig. 1(iii)).

2.1.1.1. Downstream transport. The scattered dose at point **b**, $S_{\mathbf{b}}$, can be calculated as the water kerma free-in-air at **b**, $K_{\mathbf{b}}$, times $(B_w^{\mathbf{b}} - 1)$, where $B_w^{\mathbf{b}}$ is the backscatter generated by the remaining phantom material present downstream, which can be considered as a full backscatter phantom. In order to estimate the value $B_w^{\mathbf{b}}$ at point **b**, we need to consider that B_w is a monotonous, slowly growing function of the field size and the beam's effective energy. As the thickness of region $\boldsymbol{\alpha}$

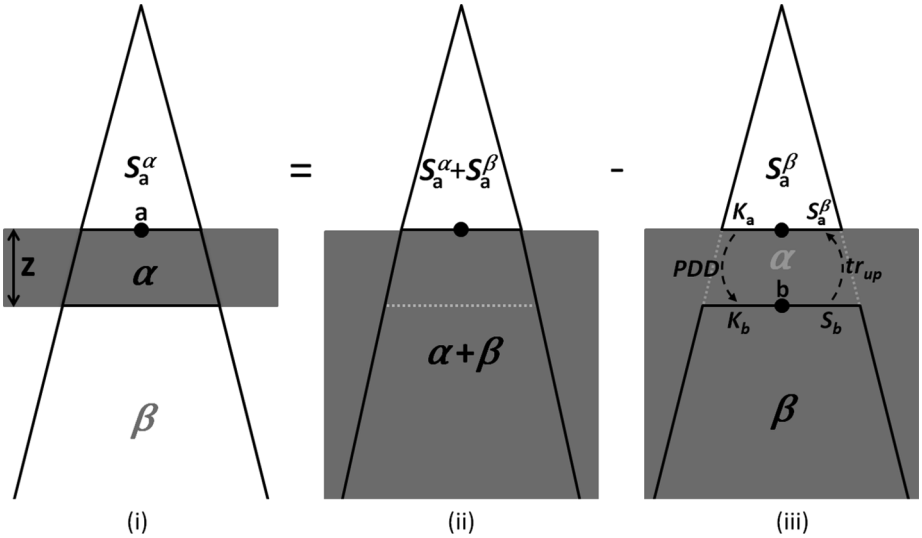

Fig. 1. Graphical representation of the physical model for calculating the loss of backscatter: The amount of backscatter received by point **a** from the irradiated volume $\boldsymbol{\alpha}$, S_a^{α} (i), can be calculated as the amount received from full backscatter conditions (ii) minus the amount received from the missing volume $\boldsymbol{\beta}$, S_a^{β} (iii).

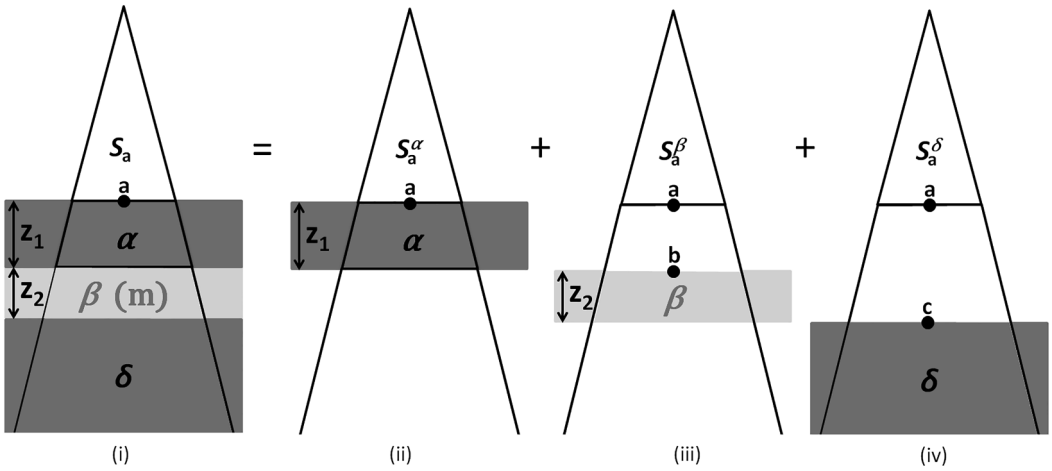

Fig. 2. Graphical representation of the physical model adapted to an heterogeneous slab phantom: (i) the amount of backscatter received by point **a** can be calculated as the amount received from each slab. Regions $\boldsymbol{\alpha}$ (ii), $\boldsymbol{\beta}$ (iii) and $\boldsymbol{\delta}$ (iv) are composed of different materials.

increases, the field size at point **b** increases (divergence) and the effective energy of the beam increases (filtration).

$K_\mathbf{b}$ can be estimated as the kerma at point **a**, $K_\mathbf{a}$, transported downwards through region $\boldsymbol{\alpha}$ to point **b**. The beam attenuation through region $\boldsymbol{\alpha}$, characterised by its thickness, z, is accounted for using the percentage depth dose of the impinging beam, $PDD(z, FS)$, where FS is the beam's field size at the phantom's surface, measured as the diameter of the equivalent circular field. With these assumptions, the scatter dose at point **b**, $S_\mathbf{b}$, is given by:

$$S_\mathbf{b} = K_\mathbf{b}(B_w^\mathbf{b} - 1) \cong K_\mathbf{a}{\cdot}PDD(z, FS){\cdot}(B_w^\mathbf{b}(z, FS_z) - 1) \tag{4}$$

where $FS_z = FS{\cdot}(SSD + z)/SSD$ is the field size at the level of point **b**.

2.1.1.2. Upstream transport. The scatter contribution from region $\boldsymbol{\beta}$ to point **a** is modelled as the scatter dose at point **b** transported upstream through region $\boldsymbol{\alpha}$:

$$S_\mathbf{a}^\beta = S_\mathbf{b}{\cdot}tr_{(z,FS)}^{up} = S_\mathbf{b}{\cdot}att(z){\cdot}g(z, FS_z) \tag{5}$$

The upstream transport factor, $tr_{(z,FS_z)}^{up}$, is modelled by the product of two functions, one accounting for the attenuation of the beam because of photon-phantom interaction, $att(z)$, and the other accounting for radiation's geometrical spread, $g(z, FS_z)$.

$att(z)$ can be considered as the infinite-SSD *PDD(z)* of a narrow beam, i.e. the *PDD* without the inverse square law component. A narrow beam geometry implies this factor is independent of field size. We used the *PDD* of a circular field of 1 cm diameter as a surrogate for narrow beam geometry.

For modelling the geometrical spread of the scattered radiation, $g(z, FS)$, we propose to treat the backscatter radiation traversing upward through the plane containing point **b** as if it were produced by identical point sources uniformly distributed on the upper surface of region $\boldsymbol{\beta}$. This assumption is based on the rapidly decreasing intensity of the impinging beam and of the backscattered radiation. This proposal implies a spatial variation of the radiation intensity that is analogous to the spatial variation of the electric field produced by a disc of uniform charge density with diameter FS_z:

$$g(z, FS_z) = \left(1 - \frac{z}{\sqrt{z^2 + FS_z{}^2}}\right) \tag{6}$$

The upstream transport factor then becomes:

$$tr_{(z,FS_z)}^{up} = PDD(z)\left(\frac{SSD + z}{SSD}\right)^2{\cdot}\left(1 - \frac{z}{\sqrt{z^2 + FS_z{}^2}}\right) \tag{7}$$

If $B_\mathbf{a}^\alpha$ represents the backscatter factor at point **a** under incomplete scatter conditions, the scatter contribution to point **a** is given by:

$$S_\mathbf{a}^\alpha = K_\mathbf{a}(B_\mathbf{a}^\alpha - 1) \tag{8}$$

Combining Eqs. (3), (4), (5), (7) and (8) we obtain the following expression for the backscatter factor under incomplete scatter conditions:

$$B_\mathbf{a}^\alpha = (B_w - 1) - PDD(z, FS){\cdot}tr_{(z,FS_z)}^{up}{\cdot}(B_w^\mathbf{b}(z, FS_z) - 1) + 1 \tag{9}$$

If we disregard the change of $B_w^\mathbf{b}$ with z (increasing field size and filtration, see Appendix 1 for justification), we can write Eq. (9) in a more compact form:

$$B_\mathbf{a}^\alpha = (B_w - 1)(1 - PDD(z, FS){\cdot}tr_{(z,FS)}^{up}) + 1 \tag{10}$$

This corrected backscatter can be used in the TG-61 formalism to calculate the dose at point **a** in incomplete scatter conditions using the formula

$$D_\mathbf{a} = K_\mathbf{a}{\cdot}B_\mathbf{a}^\alpha \tag{11}$$

Eqs. (9), (7) and (6) predict the variation of $B_\mathbf{a}^\alpha$ with changes in the thickness of the incomplete backscatter slab, the field size and beam quality, through B_w, $B_w^\mathbf{b}(z, FS_z)$, $tr_{(z,FS_z)}^{up}$ and $PDD(z, FS)$.

It is noteworthy that the model-derived algorithm (Eq. (9)) and its compact form (Eq. (10)) correctly predict the extreme situations of both a full-scatter phantom and a total lack of scattering material. This is easily seen on the compact form (Eq. (10)): For the full-scattering situation, $z = \infty$, both $PDD(z, FS)$ and $tr_{(z,FS)}^{up}$ vanish, making $B_\mathbf{a}^\alpha = B_w$. For a complete lack of backscatter material, $z = 0$, both $PDD(z, FS)$ and $tr_{(z,FS)}^{up}$ equals 1 and hence $B_\mathbf{a}^\alpha = 1$ (no backscatter).

2.1.2. Heterogeneous phantoms

The model can be easily extended to deal with heterogeneous slab phantoms. The scatter contribution to the dose at the entrance surface of the phantom from each slab can be calculated if the kerma at the upper surface of each slab, the full-backscatter factor corresponding to the slab material and the *PDD* of the impinging beam in the slab material are known. Clinical cases like the irradiation of the scalp can be modelled by such slab geometry.

The phantom depicted in Fig. 2 represents a full-scatter water phantom with a slab of a different material (medium "m") of thickness z_2 inserted at the depth z_1. The scatter at point **a** from the irradiated volume $\boldsymbol{\alpha}$ can be calculated combining Eqs. (3), (4) and (5):

$$S_\mathbf{a}^\alpha = K_\mathbf{a}{\cdot}((B_w - 1) - PDD(z, FS){\cdot}tr_{(z,FS_z)}^{up}{\cdot}(B_w^\mathbf{b}(z, FS_z) - 1)) \tag{12}$$

Table 1
Beam characteristics of the Xstrahl-100 superficial machine.

Filter code	Peak potential [kV]	Added Filtration [mm Al]	Half value layer [mm Al]
F2	50	0.8	0.8
F3	80	1.7	2.0
F5	100	1.9 (+0.05 mm Cu)	4.0

Eq. (12) can be used to compute the scatter at point **b** from the irradiated volume $\boldsymbol{\beta}$, $S_{\mathbf{b}}^{\beta}$, by replacing the full-backscatter-in-water values B_w and $B_w^{\mathbf{b}}$ with the full-backscatter-in-medium-"m" values B_m and $B_m^{\mathbf{c}}$:

$$S_{\mathbf{b}}^{\beta} = K_{\mathbf{b}}\cdot((B_m - 1) - PDD(z, FS)\cdot tr^{up}_{(z,FS_z)}\cdot(B_m^{\mathbf{c}}(z, FS_z) - 1)) \tag{13}$$

$K_{\mathbf{b}}$, the water kerma free-in-air at point **b**, can be modelled as:

$$K_{\mathbf{b}} \cong K_{\mathbf{a}}\cdot PDD(z_1, FS) \tag{14}$$

To quantify the amount of scatter reaching point **a** from region $\boldsymbol{\beta}$, we need to transport $S_{\mathbf{b}}^{\beta}$ upwards through region $\boldsymbol{\alpha}$. Eqs. (5), (6) and (7) describe this upward transport:

$$S_{\mathbf{a}}^{\beta} = S_{\mathbf{b}}^{\beta}\cdot tr^{up}_{(z_1,FS)} = S_{\mathbf{b}}^{\beta}\cdot PDD(z_1)\left(\frac{SSD + z_1}{SSD}\right)^2\cdot\left(1 - \frac{z}{\sqrt{{z_1}^2 + {FS_{z_1}}^2}}\right) \tag{15}$$

The same process allows for the calculation of the scatter contribution from region $\boldsymbol{\delta}$ to point **a**: if region $\boldsymbol{\delta}$ is thick enough to provide full-scatter conditions, the amount of scatter at point **c** is $K_{\mathbf{c}}(B_w^c - 1)$; if region $\boldsymbol{\delta}$ does not provide full-scatter, then Eq. (12) can be used to compute the scatter at point **c** from the irradiated volume $\boldsymbol{\delta}$, $S_{\mathbf{c}}^{\delta}$ by replacing $K_{\mathbf{a}}$ with $K_{\mathbf{c}}$, the water kerma free-in-air at point **c**:

$$S_{\mathbf{c}}^{\delta} = K_{\mathbf{c}}\cdot((B_w^{\mathbf{c}} - 1) - PDD(z_\delta, FS)\cdot tr^{up}_{(z_\delta,FS_{z_\delta})}\cdot(B_w^{\mathbf{c}}(z_\delta, FS_{z_\delta}) - 1)) \tag{16}$$

The water kerma free-in-air at point **c** can be modelled as:

$$K_{\mathbf{c}} \cong K_{\mathbf{b}}\cdot PDD_\beta(z_2, FS) \cong K_{\mathbf{a}}\cdot PDD(z_1, FS)\cdot PDD_\beta(z_2, FS) \tag{17}$$

where PDD_β is the *PDD* corresponding to the medium "m" filling region $\boldsymbol{\beta}$.

The amount of scatter reaching point **a** from region $\boldsymbol{\delta}$ is computed transporting $S_{\mathbf{c}}^{\delta}$ upwards through regions $\boldsymbol{\beta}$ and $\boldsymbol{\alpha}$:

$$S_{\mathbf{a}}^{\delta} = S_{\mathbf{c}}^{\delta}\cdot(tr^{up})_{\beta,\alpha} = S_{\mathbf{c}}^{\delta}\cdot PDD_\beta(z_2)\left(\frac{SSD + z_2}{SSD}\right)^2\cdot PDD_\alpha(z_1)\left(\frac{SSD + z_1}{SSD}\right)^2\cdot \left(1 - \frac{z_1 + z_2}{\sqrt{(z_1 + z_2)^2 + FS^2}}\right) \tag{18}$$

Combining the scatter to point **a** from each slab allows us to calculate the backscatter:

$$B_{\mathbf{a}} = 1 + \frac{S_{\mathbf{a}}^{\delta}}{K_{\mathbf{a}}} + \frac{S_{\mathbf{a}}^{\beta}}{K_{\mathbf{a}}} + \frac{S_{\mathbf{a}}^{\alpha}}{K_{\mathbf{a}}} \tag{19}$$

To be able to compute the backscatter at point **a,** we need to know the full-backscatter factors and the *PDD* for each medium on the slab phantom. This data is generally not available and its determination is challenging. Nonetheless, for treatments of the scalp, the problem can be well modelled by a full-scatter water phantom containing a slab of bone material. In such a case, dosimetry protocols provide values of full-scatter backscatter factors in bone and values of $(\bar{\mu}_{en}/\rho)_w^{bone}$, which can be used to scale the dimensional parameters of water PDDs in order to estimate bone PDDs. For the range of energies considered in this work, $(\bar{\mu}_{en}/\rho)_w^{bone} \cong 4$. A 1 cm slab of bone can therefore be considered as a full backscatter slab, enabling us to simplify the calculation of the backscatter at the surface to the following expression:

$$B_{\mathbf{a}} = (B_w - 1) - PDD(z_1, FS)\cdot tr^{up}_{(z_1,FS_{z_1})}\cdot(B_w^{\mathbf{b}} - B_{bone}^{\mathbf{b}}) + 1 \tag{20}$$

Table 2
Thickness of Solid Water phantom used on film measurements.

Filter code	Thickness of underlying backscatter material [mm]
F2 (HVL = 0.8 mm Al)	3, 5, 10, 20, 50
F3 (HVL = 2 mm Al)	3, 5, 10, 20, 70
F5 (HVL = 4 mm Al)	3, 5, 10, 20, 30, 70

2.2. Measurement of relative reduction of backscatter

For experimental validation of our model we used superficial X-rays generated by an Xstrahl-100 machine incident on varying thicknesses of a Gammex 457-CTG Solid Water® phantom and Gafchromic™ EBT3 films. The Xstrahl-100 contains a tungsten anode tube and is able to deliver accelerating potentials between 20 kV and 100 kV. The machine is equipped with circular open applicators of 15 cm SSD. We used a circular applicator of 6 cm diameter for all measurements reported in this work. We used three different beam qualities, referred to as F2, F3 and F5, as these are the machine's codes for the added filtration. The characteristics of these three beam qualities are listed in Table 1.

We measured the relative reduction of backscatter as a function of thickness by varying the amount of underlying Solid Water. The investigated geometries are listed in Table 2. Doses at the surface of the Solid Water phantom were assessed by irradiating three pieces of film for each investigated geometry, with the films placed at the beam central axis on the surface of the Solid Water phantom.

We calibrated the films using the F3 beam (HVL = 2 mm Al) and the 6 cm applicator in Solid Water under full-scatter conditions. The exposure time for each measurement was varied in order to have the films irradiated to a dose of approximately 5 Gy, allowing the use of a narrow calibration curve. The calibration curve contained 5 dose levels spanning a 20% variation centered on 5 Gy. A narrow calibration curve reduces the uncertainties involved in converting optical density to dose when compared to a wider calibration curve. To assess the optical density corresponding to each dose level we irradiated three pieces of film for each dose level.

All films were scanned in an Epson Expression 10000 XL scanner, and images of the films were obtained in transmission mode using a 72 dpi resolution. Each piece of film was scanned before and after irradiation at the same position on the scanner bed. A template was used to ensure the reproducibility of film placement in relation to the scanner bed. The reproducibility of film placement is important, as scanners exhibit some variability of response across the scanner bed [17]. Each image consisted of the average of 3 consecutive scans. The images corresponding to the irradiated (< irr >) and un-irradiated (< blank >) state of each film were manually registered in order to correct for possible misalignment, and these manually registered films were subsequently combined to produce a net pixel value (NetPV) image as follow:

$$\text{NetPV(pixel i)} = <\text{irr}>\text{(pixel i)}/<\text{blank}>\text{(pixel i)} \tag{21}$$

Film analysis was done using in-house multichannel film dosimetry software. Two different algorithms were used to convert NetPV to dose: weighted mean (WM) and Micke–Mayer (MM) methods [18,19]. For each algorithm we used three different sensitometric functional types: the rational function, 2nd degree polynomial and 4th degree polynomial. The reported dose values corresponding to each measurement set-up are the average dose calculated on the central 17 pixel × 17 pixel region of each of the three films used per experimental set-up, assessing the dose per pixel with the 6 different methods previously described. The estimated overall uncertainty for the dose values determined using films is ± 1% (2 σ). Uncertainty in the weighted mean (WM) and Micke–Mayer (MM) algorithms are well characterised by the authors [18,19]. We combined in quadrature the uncertainty from each measurement of net optical density and dose conversion algorithm for

calculating the reported estimated uncertainty.

2.3. Monte Carlo modelling

We used EGSnrc RZ user code for all MC simulations presented in this work [20,21]. We used the source type 1 (point source) for simulating X-ray beams impinging on the geometries listed in Table 2. This source type allows the user to define the spectra, source-phantom distance (SSD) and radius of a circular field size at the phantom's entrance surface.

The following radiation transport parameters were common to all simulations: PRESTA-II electron-step algorithm, coherent Rayleigh scattering "On", photo-electron angular sampling "On", "Simple" bremsstrahlung sampling, electron-impact ionization "On", "Exact" boundary crossing algorithm (skin depth = 3), bound Compton scattering "On", ECUT = 0.521 MeV, PCUT = 0.001 MeV, atomic relaxations "On", ESTEPE = 0.25, Xlmax = 0.5 and spin effects "On". The surface dose was scored in a cylinder of 0.2 mm depth and 5 mm radius.

We used between 2×10^8 and 5×10^9 histories per simulation, depending on the field size (0.5 cm diameter up to 10 cm diameter), allowing us to have less than 1% statistical uncertainty for surface doses. The spectra of the X-ray beams were determined using TASMICS (Tungsten Anode Spectral Model using Interpolating Cubic Splines) [22]. TASMICS produces X-ray spectra with 1 keV energy resolution for minimally inherently filtered (0.8 mm Be) beams traversing user-defined added filtration. The spectra generation parameters were fine-tuned to match the HVL of the beams being studied. The quality of the MC simulations was assessed by comparing MC-generated *PDD*s with *PDD* data published in the British Journal of Radiology Supplement 25 (BJR-Sup25) and MC-generated B_w values with published data (TG-61) [3,4]. In Appendix 2 we present the validation of our MC simulations by comparison with published data.

3. Results

3.1. Comparison of film-measured, Monte Carlo-calculated and model-predicted backscatter factors

We measured the relative reduction of backscatter at the surface of a Solid Water phantom (point **a**) for three different beam qualities available on our machine, F2, F3 and F5 (Table 1), and for varying thicknesses of region $\boldsymbol{\alpha}$ (Fig. 1(i)), as per the experimental set-ups given in Table 2.

We calculated the relative reduction of backscatter with a corresponding reduction of scattering material, expressed as the quotient $B_{\mathbf{a}}^{\alpha}$ (thickness)/B_w (full-scatter). In order to do this, we used the compact form of the equation describing the model introduced in this work (Eq. (10)), values taken from backscatter tables inTG-61 and PDD data from BJR-Sup25. We also calculated the reduction of backscatter factor for the same experimental set-ups using the MC methodology described above.

The comparison of the relative reduction of backscatter as a function of phantom thickness presented in Fig. 3 reveals a high degree of agreement between the values predicted using the model introduced in this work, the film-measured and MC-calculated values: the differences between the model-predicted and MC-calculated values are of the same magnitude as the MC statistical uncertainty (± 0.5%).

3.2. Comparison of model-predicted backscatter factors with published data-fitting formula

We compared the predictions of our model (compact form, Eq. (10)) with values derived from the data-fitting formulas provided by Klevenhagen using the methodology discussed in Section 3.1 [11]. This comparison is presented in Fig. 3; it reveals a poorer degree of agreement than that discussed in the previous section. The values predicted using the model introduced in this work are consistently bigger than the ones predicted using Klevenhagen's data-fitting formulas. The same discrepancy has been reported by Eaton et al and Healy et al. [8,10].

Klevenhagen presented the reduction of backscatter defining the parameter *FFBS* as "the fraction of the full backscatter" and proposed the following data-fitting formula for this parameter [11]:

$$FFBS(z) = 1 - e^{-\frac{z}{k}} \tag{22}$$

Klevenhagen's paper does not give a clear definition of *FFBS*, but considering this parameter varies between 0 and 1, we concluded this parameter is actually a quotient between the scattered component of in-phantom doses, i.e, $(B_{(z)} - 1)/(B_w - 1)$, the same interpretation was published by Lanzon et al. [23]. By combining Eq. (10) with Eq. (22), we can derive an expression for *FFBS* based on our model's calculation algorithm:

$$\begin{aligned} FFBS(z) &= (1 - PDD(z, FS)\cdot tr^{up}_{(z,FS)}) \\ &= \left(1 - \left(\frac{SSD}{SSD + z}\right)^2\left(1 - \frac{z}{\sqrt{z^2 + FS_z{}^2}}\right)e^{-\frac{z}{\tau}}\right) \end{aligned} \tag{23}$$

On Eq. (23), the variation of *PDD* with z can be expressed as a geometric spreading function (inverse square law) times an exponential attenuation factor, $e^{-\mu z}$ [24]. The $tr^{up}_{(z,FS)}$ factor, defined on Eq. (7), can also be expressed as an exponential attenuation factor times a geometric factor. The prediction of *FFBS* in our model is different from Klevenhagen's data-fitting formula due to the positive defined geometric factor which is smaller than 1 for $z > 0$ cm and for any *FS* or *SSD*. This can explain the differences observed between our model (and modern published data) with Klevenhagen's data-fitting formula.

3.3. Comparison of model-predicted backscatter factors with published data and Monte Carlo- calculated data

Fig. 4 shows values of the relative reduction of backscatter with reduction of scattering material calculated using the model introduced in this work and values published by Healy et al. [10,25]. Our model correctly predicts the measured values, corresponding to 3 different beam qualities, with a maximum difference of 1%.

Fig. 5, panel A presents the values of the relative reduction in backscatter as a function of field size as predicted by our model and the values published by Healy et al. for a 1 cm thick phantom. The same trend is observed by our model and the published values. Some discrepancies are observable but the maximum difference does not exceed 1%.

In Fig. 5, panel B, we present the same model-predicted values compared with our own MC-calculated values. In this case we can observe better agreement between the two sets of values. This is probably the result of the fine-tuned spectra used in our MC calculation, which allowed us to correctly reproduce the *PDD* and B_w data that was used to compute backscatter reduction using the model-based algorithm.

3.4. Comparison of model-predicted backscatter factors with published data for a water/bone slab phantom

We compared the predictions of our model in the case of a slab of bone material inserted in a water phantom (Eq. (20)), with data published by Baines et al. [6]. Baines et al. investigated the reduction of backscatter with the decrease in water-equivalent scattering medium with air as the underlying material (Fig. 6A/Eq. (10)) and with the presence of a bone slab as the underlying material (Fig. 6B/Eq. (20)).

Fig. 7 constitutes a comparison of the predictions of our model with their published data corresponding to MC-calculated values of the relative reduction of backscatter, as a function of water-phantom thickness or depth to the bone slab (slab thickness = 1 cm), for the 150 kV beam and for 2 different field sizes [26].

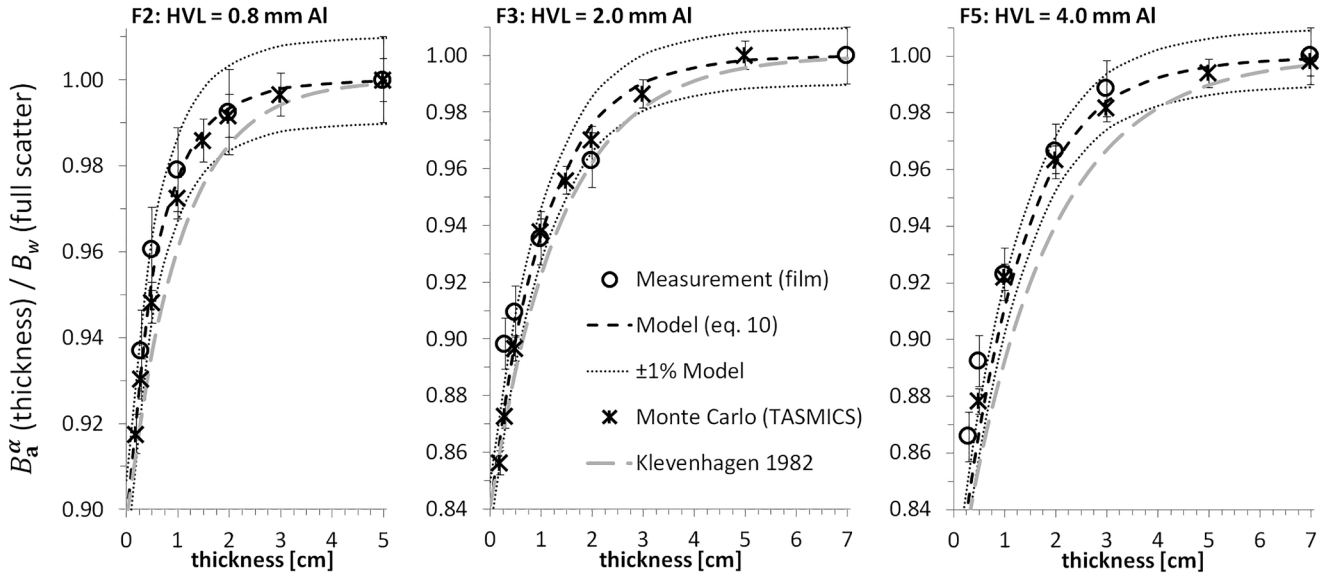

Fig. 3. Comparison of measured (○), model-predicted (– –), Klevenhagen's data-fitting formula (——) and MC calculated (*) reduction of backscatter due to loss of backscatter material, expressed as the quotient B_a^α (thickness)/B_w (full-scatter). The data corresponds to 3 different beam qualities and for a 6 cm diameter applicator (SSD = 15 cm) on a water equivalent phantom of varying thickness. The fine dotted lines represent the region of ± 1% variation of the B_a^α/B_w quotient as calculated using the model introduced on this work.

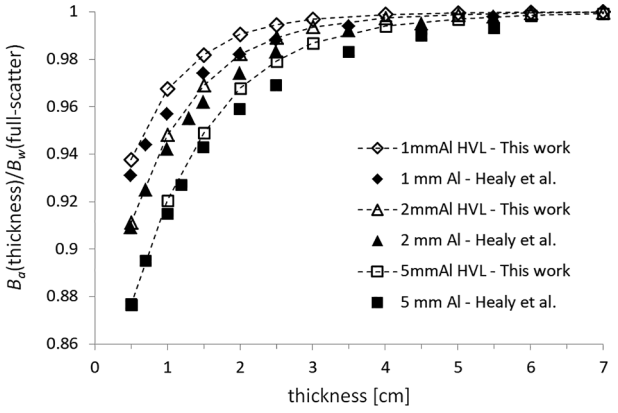

Fig. 4. Comparison of relative reduction of backscatter at the surface of a water phantom, for 3 different beam qualities and for varying phantom thicknesses (thickness of region $\boldsymbol{\alpha}$) as predicted by the model introduced on this work (Eq. (10), filled symbols) and published by Healy et al. (open symbols).

4. Discussion

The high degree of agreement of model-predicted values with measured, MC-calculated and previously published data validates the suitability of the proposed model. In particular, the compact forms of the algorithm, expressed by Eq. (10) (homogeneous phantom) and Eq. (20) (bone slab in full-scatter water phantom) succeeded in predicting the loss of backscatter with clinically suitable precision.

The compact form expressed in Eq. (10), describing the proposed model disregarding the change of B_w with *FS* and beam spectrum, correctly describes the variation of B_a^α with the thickness of the scattering material, with the variation of beam quality and with variation of field size. Poorer agreement was observed with Klevenhagen's data-fitting formula [11]. We suspect the empirical model presented by Klevenhagen does not accurately model the geometric radiation spread component. This is apparent in the lack of agreement in the middle section of the curve.

The model extension for heterogeneous slab phantoms (Eq. (20)) predicts backscatter reduction for difficult-to-manage clinical situations in close concordance with published MC data, further indicating that

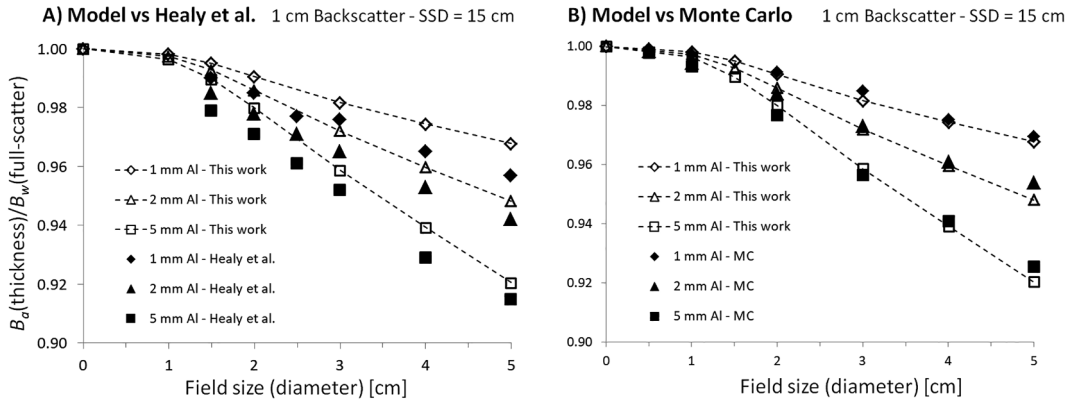

Fig. 5. Comparison of the relative reduction of backscatter at the surface of a 1 cm thick water phantom, for 3 different beam qualities and for varying field sizes: A) Predicted by the model introduced on this work (Eq. (10), open symbols) vs data published by Healy et al. (filled symbols), B) Predicted by the model introduced on this work (Eq. (10), open symbols) vs MC calculation (filled symbols).

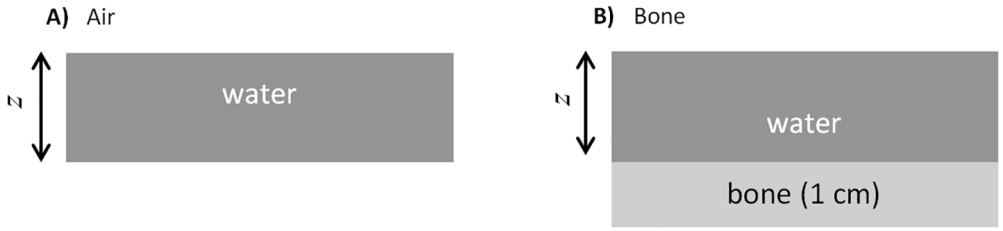

Fig. 6. Schematic of the phantom used in the investigation by Baines et al.: A) water phantom of varying thicknesses, B) water phantom of varying thicknesses with a 1 cm thick bone slab at the bottom. In both cases the beam is directed downwards to the upper surface.

the physical model successfully incorporates the dominant mechanisms of backscatter production and transport.

Changed scattering conditions occur due to the use of lead shielding to spare underlying healthy tissue. The presence of lead shielding results in a reduction of scattered radiation due to the dramatically increased beam attenuation in lead. The resulting dose reduction is similar to cases with missing underlying scattering material as the presence of lead results in the loss of backscatter radiation from underlying shielded tissues. The corresponding dose reduction is accurately modelled by our algorithm. Nevertheless, a localised dose enhancement in areas very close to lead shielding (closer than a millimetre) has been reported [8,10,27,28]. The effect of dose enhancement in areas very close to lead shielding is not modelled by our algorithm, however, published data shows this effect is less prominent at clinically relevant distances than the dose reduction due to the lack of backscatter produced by the lead shield [8,10,27,28]. In clinical practice lead shielding is covered with plastic wrap or wax in order to avoid direct contact between the lead and patients' tissues; this mitigates the effect of localised dose enhancement. Mayles et al. state 1 mm of wax is sufficient to mitigate the effect of localised dose enhancement due to lead up to 140 kV but no reference is provided to justify this [28]. However, Das and Chopra suggest that 1 mm of tissue equivalent material is sufficient up to 300 kV [27].

Our model, as expressed in Eqs. (10) and (20), can be used clinically without further gathering of experimental data and has the potential to increase the accuracy of clinical dosimetries.

The model employs a heuristic determination of the backscattered radiation's effective energy. The effect of varying the energy of backscattered radiation is explicitly investigated in Appendix 1. The broad beam attenuation factors used in this semi-empirical model were deduced from published *PDD* data. Upstream backscattered radiation was considered as originating from a two-dimensional disc of uniformly distributed equal-intensity point sources. The experimental data was measured using films in Solid Water, while modelled values are calculated from published *PDD* and B_w values for water. The impact of these assumptions has been considered in the uncertainties given in this report.

5. Conclusions

This work provides a simple model of the physical mechanisms that result in the reduction of backscatter due to missing underlying tissue in superficial X-ray radiation therapy. The algorithm allows an intuitive understanding of the effects of field size and beam energy.

The algorithm accurately predicts the effect of partial scatter conditions in superficial X-rays with accuracy appropriate for clinical applications. Its precision, combined with the simplicity of calculation, makes this methodology suitable to be incorporated into routine clinical dosimetry.

6. Compliance with ethical standards

Conflict of Interest: The authors declare that they have no conflict of interest.

Ethical approval: This article does not contain any studies with human participants or animals performed by any of the authors.

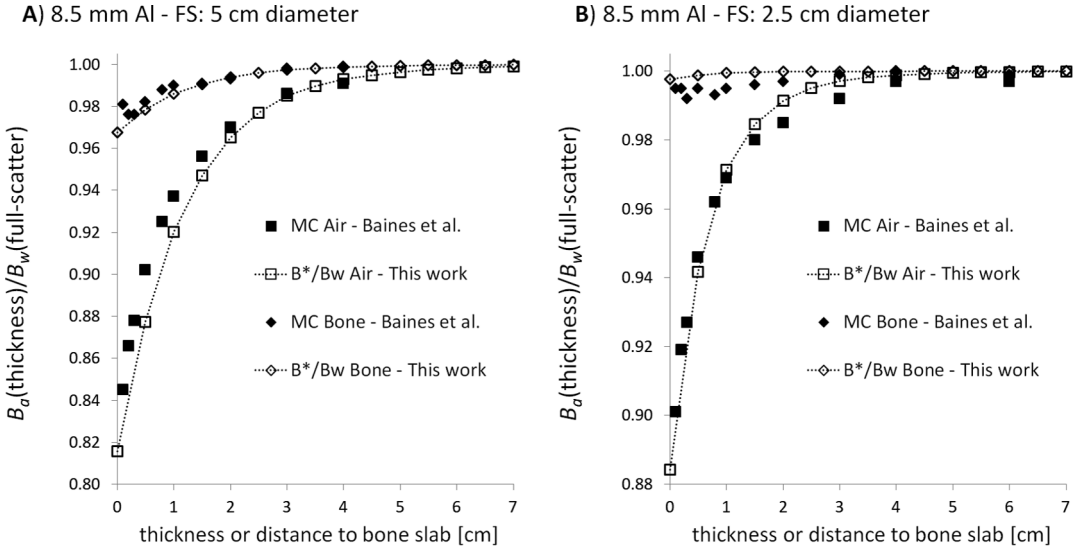

Fig. 7. Comparison of relative reduction of backscatter at the surface of a water phantom, with and without a 1 cm thick bone slab, for 2 different beam qualities and 2 field sizes, as a function of phantom thickness or distance to the bone slab: Predicted by the model introduced on this work (Eq. (10) – Air, Eq. (20) – Bone, open symbols) vs MC-calculated data published by Baines et al. (filled symbols). A) 5 cm diameter field size, B) 2.5 cm diameter field size.

Appendix 1

Characterisation of model parameters

The energy spectrum and the field size of the beam at point **b** are functions of the thickness of region ***α*** (see Fig. 4). As the thickness of region ***α*** increases, the field size at point **b** increases linearly and the effective energy of the beam increases (filtration). Beam hardening because of increased filtration as z increases produces less than 1% change in B_w for a 100 kV beam traversing 7 cm of water, and can therefore be ignored. We determined a maximum difference of less than 0.5% on the estimation of the relative reduction of the backscatter factor when disregarding the change of B_w because of this effect. The change of B_w with field size is easily manageable and has been incorporated into the model-based values reported in this work.

The transport of scattered radiation upstream requires the evaluation of the beam transmission properties of the phantom material, $att(z)$. This parameter is modelled as the infinite-SSD *PDD(z)*. In order to evaluate $att(z)$ we need to know the quality of the scattered radiation.

We estimated the beam quality of the scattered radiation in the following way: using μ/ρ NIST data for aluminium and mono-energetic photon beams, we calculated an "effective beam energy" for our F2, F3 and F5 beams. This was defined as the energy of the mono-energetic beam displaying the same aluminium HVL: HVL = $0.63/\mu$ [24]. We used the prediction of change of energy of the recoiling photon in Compton scattering theory to compute the change in effective energy for scattering at 90 degrees and 180 degrees. We used this "effective energy" of the recoiling photons and μ/ρ NIST data to compute the HVL of the scattered radiation. The results are presented in Table 3:

Table 3
Estimation of beam quality of backscattered radiation.

	Incident beam		90° Scatt.		180° Scatt.	
	Eff. E [keV]	HVL [mm Al]	Eff. E [keV]	HVL [mm Al]	Eff. E [keV]	HVL [mm Al]
F2	20.2	0.8	19.5	0.72	18.8	0.64
F3	28.6	2.0	27.1	1.75	25.7	1.53
F5	38.3	4.0	35.7	3.39	33.4	2.90

The change in beam quality of the scattered radiation affects the calculation of the reduction of backscatter factor through its impact on the estimation $att(z)$. Fig. 8 presents the maximum expected change in $att(z)$ and $tr^{up}_{(z,FS_z)}$ for a 5 cm diameter F2 and F5 beam both when considering and disregarding the change in beam quality of the backscattered radiation. Despite the maximum change in the estimated value of attenuation amount of 20%, the rapid reduction of the geometric part of the upward transmission, $g(z, FS_z)$ (Eq. (6)) produces a minimal difference on the overall upward transmission coefficient, $tr^{up}_{(z,FS_z)}$. This results in a maximum difference of less than 0.5% on the estimation of the relative reduction of the backscatter factor when disregarding the change in beam quality of the scattered radiation.

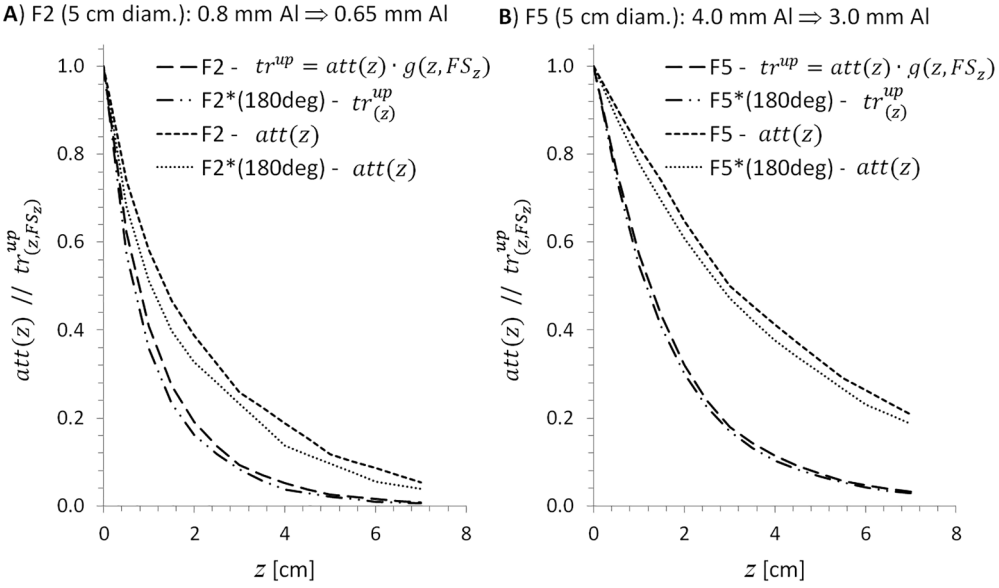

Fig. 8. Maximum expected change in att(z) and $tr^{up}_{(z,FS_z)}$ for a 5 cm diameter F2 and F5 beam when considering (F2*(180 deg), F5*(180 deg)) or disregarding (F2, F5) the change in beam quality of the backscattered radiation: Panel **A** corresponds to the F2 beam and panel **B** corresponds to the F5 beam.

Appendix 2

Comparison of MC-calculated dosimetric parameters with published data

We assessed the quality of our MC simulations by comparing our MC-predicted *PDD* and B_w values with published data. We calculated *PDD* data

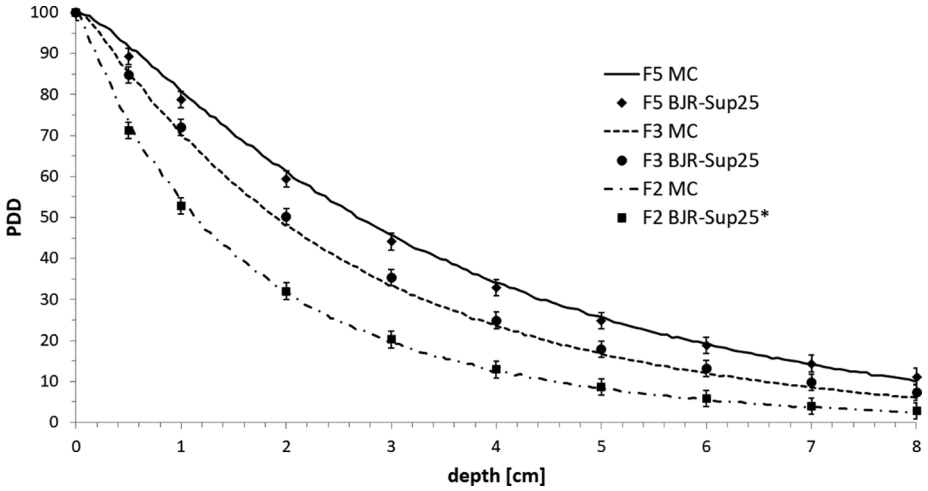

Fig. 9. Comparison of MC-generated *PDD*s and BJR-Sup25 published data for 3 different beam qualities: F2 (0.8 mm Al), F3 (2.0 mm Al) and F5 (4.0 mm Al). The ± 2% error bars on the BJR-Sup25 data are only indicative of the degree of conformity with the MC-generated data.

for the F2, F3 and F5 beams using the TASMICS spectra, which were fine-tuned to match the measured HVLs. We used an SSD of 15 cm and a circular field size of 5 cm diameter.

Fig. 9 presents a comparison between the MC-calculated *PDD*s and the data published in the BJR-Sup25. The published data is displayed with accompanying ± 2% error bars. This uncertainty does not represent the uncertainty of the BJR-Sup25 data but is an indication of the degree of conformity with the MC-generated data: the average difference between these data, referenced to the 100% level, was 1.1% (σ = 0.8%) and the maximum discrepancy was 2.7% (difference calculated as: (MC(z)[%]-BJR-Sup25(z)[%])/100%.). For the F3 and F5 beams, there is *PDD*-published data corresponding to their HVL. For the F2 beam (HVL = 0.8 mm Al), however, there is no data with an identical HVL. We therefore obtained the *PDD* of the F2 beam from BJR-Sup25 published data for HVL = 0.7 mm Al and for HVL = 1.0 mm Al, using a linear interpolation [4]. Published data was used as measurement of *PDD*s has a comparable or greater degree of uncertainty than published data especially for tube potentials below 40 kVp [3].

We calculated B_w values from MC simulations by calculating the dose per incident particle deposited on a water-filled disc of 1 cm diameter by 0.2 mm height, positioned on the beam-entrance face of a 15 cm diameter by 15 cm height cylindrical phantom filled with water, D_w, or with air, D_{air}, delivering enough particles to ensure an uncertainty of less than 0.5% of the scored dose.

The B_w value was calculated as the quotient D_w/D_{air}. This quotient is not exactly B_w, as the latter is defined as the quotient of kerma in water in a full-scatter water phantom, divided by the kerma in water free-in-air. Nonetheless, D_w/D_{air} represents a very good approximation of B_w, as back-scatter in the water-filled disc used as surrogate of a water-filled volume just big enough for ensuring charged particle equilibrium generates a negligible amount of scattered radiation, thus fulfilling the TG-61 provisions [3]. The absorbed dose to water, D_w, at the water surface can be approximated by K_w with the assumption of the existence of charged particle equilibrium and the negligible difference between kerma and collision kerma. We simulated a circular field of 6 cm diameter with SSD = 15 cm.

TG-61 states a 1.5% uncertainty (1σ) for B_w; the values of B_w we calculated have a numerical uncertainty of 1% (1σ). The small differences stated in Table 4 support the quality of our simulations. In particular, they support the validity of our method of calculating backscatter factors. It is to be noted that the magnitude we are studying is a quotient of backscatter factors, thus the impact of small deviations observed between our B_w values, deduced from our simplistic MC-simulations, and published values is therefore very likely minimal.

Table 4
B_w values for a 6 cm circular field at SSD = 15 cm. MC: Monte-Carlo generated data, TG-61: TG-61 published data. The percent difference was calculated as 100 (MC-TG-61)/TG-61.

	MC	TG61	Diff%
F2	1.134	1.115	1.7
F3	1.213	1.190	1.9
F5	1.254	1.240	1.1

Supplementary data

Supplementary data to this article can be found online at https://doi.org/10.1016/j.ejmp.2019.08.018.

References

[1] Aukett RJ, Burns JE, Greener AG, Harrison RM, Moretti C, Nahum AE, et al. Addendum to the IPEMB code of practice for the determination of absorbed dose for x-rays below 300 kV generating potential (0.035 mm Al-4 mm Cu HVL). Phys Med Biol 2005;50:2739–48. https://doi.org/10.1088/0031-9155/50/12/001.

[2] Klevenhagen SC, Aukett RJ, Harrison RM, Nahum AE, Rosser KE. The IPEMB code of practice for the determination of absorbed dose for x-rays below 300 kV generating potential (0. 035 mm Al – 4 mm Cu HVL; 10–300 kV generating potential). Phys Med Biol 1996;41:2605. https://doi.org/10.1088/0031-9155/41/12/002.

[3] Ma C-M, Coffey CW, DeWerd LA, Liu C, Nath R, Seltzer SM, et al. AAPM protocol for 40–300 kV x-ray beam dosimetry in radiotherapy and radiobiology. Med Phys 2001;28:868–93. https://doi.org/10.1118/1.1374247.

[4] British Institute of Radiology/Institute of Physics and Engineering in Medicine and Biology. Central axis depth dose data for use in radiotherapy, 1996 : a survey of

depth doses and related data measured in water or equivalent media. British Institute of Radiology; 1996.
[5] Hill R, Healy B, Butler D, Odgers D, Gill S, Lye J, et al. Australasian recommendations for quality assurance in kilovoltage radiation therapy from the Kilovoltage Dosimetry Working Group of the Australasian College of Physical Scientists and Engineers in Medicine. Aust Phys Eng Sci Med 2018. https://doi.org/10.1007/s13246-018-0692-1.
[6] Baines J, Zawlodzka S, Markwell T, Chan M. Measured and Monte Carlo simulated surface dose reduction for superficial X-rays incident on tissue with underlying air or bone. Med Phys 2018;45:926–33. https://doi.org/10.1002/mp.12725.
[7] Kim J, Hill R, Claridge Mackonis E, Kuncic Z. An investigation of backscatter factors for kilovoltage x-rays: a comparison between Monte Carlo simulations and Gafchromic EBT film measurements. Phys Med Biol 2010;55:783–97. https://doi.org/10.1088/0031-9155/55/3/016.
[8] Eaton DJ, Doolan PJ. Review of backscatter measurement in kilovoltage radiotherapy using novel detectors and reduction from lack of underlying scattering material. J Appl Clin Med Phys 2013;14:5–17. https://doi.org/10.1120/jacmp.v14i6.4358.
[9] Hill R, Healy B, Holloway L, Kuncic Z, Thwaites D, Baldock C. Advances in kilovoltage x-ray beam dosimetry. Phys Med Biol 2014;59. https://doi.org/10.1088/0031-9155/59/6/R183.
[10] Healy BJ, Sylvander S, Nitschke KN. Dose reduction from loss of backscatter in superficial x-ray radiation therapy with the Pantak SXT 150 unit. Aust Phys Eng Sci Med 2008;31:49–55. https://doi.org/10.1007/BF03178453.
[11] Klevenhagen SC. The build-up of backscatter in the energy range 1 mm Al to 8 mm Al HVT (radiotherapy beams). Phys Med Biol 1982;27:1035–43. https://doi.org/10.1088/0031-9155/27/8/005.
[12] Radiation Oncology Tripartite Committee. Planning for the best: tripartite national strategic plan for radiation oncology 2012–2022. R Aust New Zeal Coll Radiol 2012.
[13] The Royal College of Radiologists. A review of the use of radiotherapy in the UK for the treatment of benign clinical conditions and benign tumours. Clin Oncol 2015. https://doi.org/10.1108/978-1-78714-831-420171008.
[14] Borras JM, Lievens Y, Grau C. The need for radiotherapy in Europe in 2020: not only data but also a cancer plan. Acta Oncol (Madrid) 2015;54:1268–74. https://doi.org/10.3109/0284186X.2015.1062139.
[15] McGregor S, Minni J, Herold D. Superficial radiation therapy for the treatment of nonmelanoma skin cancers. J Clin Aesthet Dermatol 2015;8:12–4.
[16] The range in liquid water of 300 keV electrons is 0.08421 g/cm2, calculated using the continuous slowing down approximation. Source: NIST – ESTAR database, https://physics.nist.gov/PhysRefData/Star/Text/ESTAR.html; n.d.
[17] Paelinck L, De Neve W, De Wagter C. Precautions and strategies in using a commercial flatbed scanner for radiochromic film dosimetry. Phys Med Biol 2007;52:231–42. https://doi.org/10.1088/0031-9155/52/1/015.
[18] Méndez I, Peterlin P, Hudej R, Strojnik A, Casar B. On multichannel film dosimetry with channel-independent perturbations. Med Phys 2014;41:011705https://doi.org/10.1118/1.4845095.
[19] Mayer RR, Ma F, Chen Y, Miller RI, Belard A, McDonough J, et al. Enhanced dosimetry procedures and assessment for EBT2 radiochromic film. Med Phys 2012;39:2147. https://doi.org/10.1118/1.3694100.
[20] Rogers DWO, Kawrakow I, Seuntjens JP, Walters BRB, Mainegra-Hing E. NRC user codes for EGSnrc. NRCC Rep PIRS-702. Rev B 2013;702:1–92.
[21] Kawrakow I, Rogers DWO. The EGSnrc code system. NRC Rep PIRS-701, NRC, Ottawa; 2000.
[22] Hernandez AM, Boone JM. Tungsten anode spectral model using interpolating cubic splines: unfiltered x-ray spectra from 20 kV to 640 kV. Med Phys 2014;41:042101https://doi.org/10.1118/1.4866216.
[23] Lanzon PJ, Sorell GC. The effect of lead underlying water on the backscatter of X-rays of beam qualities 0.5 mm to 8 mm Al HVT. Phys Med Biol 1993;38:1137–44. https://doi.org/10.1088/0031-9155/38/8/012.
[24] Khan FM. The Physics of Radiation Therapy. Williams & Wilkins; 1994.
[25] We extracted the values from a pdf version of Healy's paper using the free, web-based tool "WebPlotDigitizer" (http://arohatgi.info/WebPlotDigitizer/app3_12/) created by Ankit Rohatgi; n.d.
[26] Dr. John Baines kindly shared with us the measured PDD of his 150 kV beam. We used his published HVL value, together with the PDD data, as input for our model; n.d.
[27] Das IJ, Chopra KL. Backscatter dose perturbation in kilovoltage photon beams at high atomic number interfaces. Med Phys 1995;22:767–73. https://doi.org/10.1118/1.597594.
[28] Mayles P, Nahum A, Rosenwald JC. Handbook of radiotherapy physics: theory and practice. Taylor & Francis; 2010.